Quasi-static and dynamic magnetic tension forces in arched, line-tied magnetic flux ropes

C E Myers, M Yamada, H Ji, J Yoo, J Jara-Almonte, and W Fox

Princeton Plasma Physics Laboratory, Princeton, New Jersey 08543, USA

5 September 2016

Abstract.

Solar eruptions are often driven by magnetohydrodynamic instabilities such as the torus and kink instabilities that act on line-tied magnetic flux ropes. Recent laboratory experiments designed to study these eruptive instabilities have demonstrated the key role of both dynamic [Myers et al., *Nature* **528**, 526 (2015)] and quasi-static [Myers et al., *Phys. Plasmas*, submitted (2016)] magnetic tension forces in contributing to the equilibrium and stability of line-tied magnetic flux ropes. In this paper, we synthesize these laboratory results and explore the relationship between the dynamic and quasi-static tension forces. While the quasi-static tension force is found to contribute to the flux rope equilibrium in a number of regimes, the dynamic tension force is significant mostly in the so-called failed torus regime where magnetic self-organization events prevent the flux rope from erupting.

(Some figures in this article are in colour only in the electronic version)

Submitted to: *Plasma Phys. Control. Fusion*

1. Introduction

The magnetic tension force is a fundamental restoring force that contributes to the equilibrium and stability of toroidal magnetohydrodynamic systems. The tension force of interest in this paper is generated by the toroidal curvature of the magnetic field. This toroidal field tension force contributes to the equilibrium of fusion devices such as the tokamak [1,2], and it has recently been shown to play a key role in both the equilibrium and stability of solar-relevant line-tied magnetic flux ropes [3, 4]. In the case of the line-tied flux rope, two tension force contributions have been identified: (1) a quasi-static tension force that contributes to the flux rope equilibrium; and (2) a dynamic tension force that can exceed the quasi-static term and prevent the flux rope from erupting. In this paper, we analyze the relationship between these two tension force contributions, which were originally reported in Refs. 4 and 3, respectively.

A line-tied magnetic flux rope is an arched bundle of helical magnetic field lines and confined plasma that is anchored, or line-tied, at two fixed footpoints. Line-tied flux ropes are found most notably in the solar corona where they store large amounts of magnetic energy for long periods of time [5–10]. This stored energy is suddenly and catastrophically released during solar eruptive events [11, 12], which are of great interest due to their role in generating space weather in Earth's magnetosphere [13]. Many solar eruptive events are thought to be driven by ideal magnetohydrodynamic instabilities such as the kink [14–17] and torus instabilities [18, 19]. Predicting if and when these instabilities can trigger an eruption, however, remains an area of active research.

Traditionally, ideal magnetohydrodynamic instabilities in the corona are studied with a combination of remote observations [20–25] and numerical modeling [26–31]. While substantial progress has been made, additional research is required to fully understand instability-driven flux rope eruptions. To this end, a dedicated laboratory experiment has recently been developed to study the torus and kink instabilities in a well-controlled laboratory setting [3, 4, 32]. This experiment is the first to generate long-lived laboratory magnetic flux ropes that evolve in a quasi-static equilibrium with the possibility of erupting due to either the kink or the torus instabilities. In this paper, we synthesize the key results of this experiment, which demonstrate the role of the toroidal field tension force both in setting the quasi-static equilibrium of the flux rope and in preventing certain flux ropes from erupting. The paper is organized as follows: In Section 2, the laboratory setup is briefly introduced along with an experimental characterization of the torus and kink instability parameter space. Then, in Section 3, direct measurements of the quasi-static and dynamic magnetic tension forces are presented. The relative amplitudes and parameter dependence of these tension force contributions are compared. We end with a brief summary and discussion in Section 4.

2. Laboratory setup and results on flux rope stability

The laboratory experiments reported in this paper are conducted in the Magnetic Reconnection Experiment (MRX) [33] at Princeton Plasma Physics Laboratory. The experimental setup is described extensively elsewhere [3, 4, 32], so we only briefly review it here. A custom-built apparatus comprised of two electrodes mounted on a glass substrate and two sets of magnetic field coils is inserted into the MRX device to produce the line-tied flux rope plasmas. Four independent magnetic field coil sets are used to produce a variety of

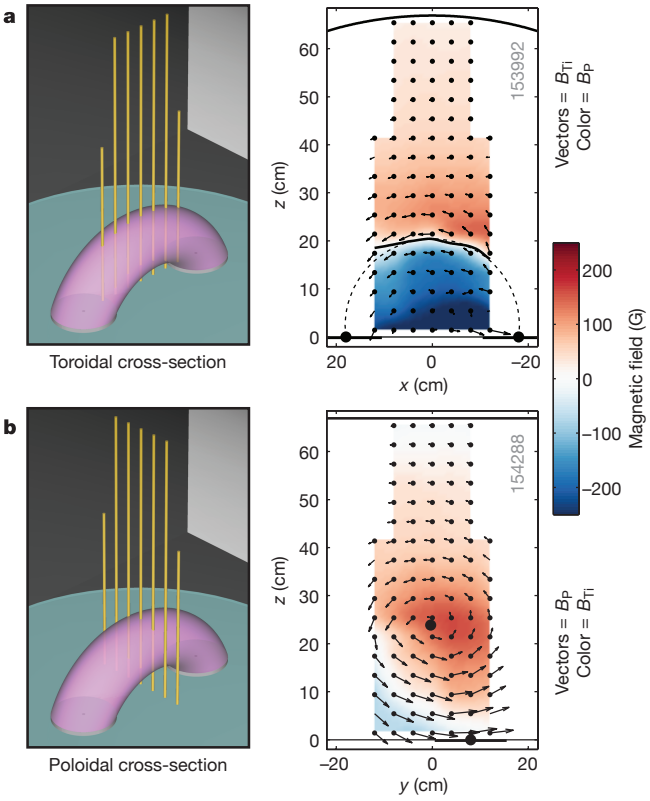

Figure 1. Laboratory setup and magnetic probe geometry for the line-tied flux rope experiments. Seven linear magnetic probes (yellow) extend vertically into the flux rope plasma (pink). Magnetic measurements acquired in the (a) toroidal and (b) poloidal cross-sections of the rope are shown on the right. In each case, the vectors represent the in-plane field, while the colors represent the out-of-plane field. The magnetic axis is located at the reversal point of the poloidal magnetic field, $B_P = B_y$. The toroidal field shown here is the plasma-produced internal field, B_{Ti}, which is paramagnetic with respect to the vacuum guide field, B_g. This figure reprinted with permission from Ref. 3.

vacuum (potential) field configurations. These vacuum fields are comprised of 'guide field' components that run toroidally along the flux rope and 'strapping field' components that run orthogonally to the rope. Once the vacuum field has been created, a capacitor bank breaks down the flux rope plasma. Non-potential magnetic energy is driven by the capacitor bank into the flux rope on a timescale of 150 μs, which is two orders of magnitude longer than the dynamic Alfvén time ($\tau_A \sim 3$ μs) and substantially shorter than the resistive diffusion time ($\tau_R \sim 500$ μs). While these are not the first laboratory experiments to produce arched line-tied flux ropes [34–36], they are the first to achieve this crucial separation of timescales, which mirrors the separation of timescales in the solar corona [12].

The MRX flux rope plasmas are diagnosed with a distributed, *in situ* magnetic probe array (see Fig. 1). The probe array is comprised of seven linear probes that are inserted vertically into the plasma. Inside each linear probe, miniature magnetic pickup coils are grouped in orthogonal sets of three at 4 cm intervals. Since the probes are also spaced horizontally at 4 cm intervals, the probe array measures all three components of the vector magnetic field on a 4 cm × 4 cm grid. The probe array can be rotated between discharges to acquire magnetic field data from various cross-sections of the flux rope.

One key measurement provided by the probe array is the flux rope magnetic axis height. This is determined by finding the location where the poloidal magnetic field, $B_P = B_y$, reverses sign (see Fig. 1). This information can be used to construct a height-time plot for each flux rope discharge (see Fig. 2). The subpanels in Fig. 2b show the height of the flux rope apex, $z_{ap}(t)$, overlaid on the measured poloidal magnetic field, $B_P(t, z)$. In each discharge the plasma current is nominally the same (Fig. 2a), but the height-time evolution varies widely. This is because the vacuum magnetic field configuration has been modified in each case in order to explore the torus versus kink instability parameter space.

The stability criteria for the torus [18, 19, 30, 37–41] and kink [14–17, 26–29] instabilities form a two-dimensional instability parameter space that can be studied in the laboratory. The torus instability is parameterized by the vacuum field decay index,

$$n(z) \equiv -\frac{z}{|\mathbf{B}_{vac}|}\frac{\partial|\mathbf{B}_{vac}|}{\partial z} > \frac{3}{2}, \tag{1}$$

where $\mathbf{B}_{vac}$ is the vacuum magnetic field and z is the height above the footpoints. The decay index quantifies how quickly the vacuum field, which provides the restoring forces on the flux rope, decays with height. If the restoring forces decay too quickly (high n), then the flux rope experiences a so-called loss-of-equilibrium and erupts. The kink instability, on the other hand, is parameterized by the edge safety factor,

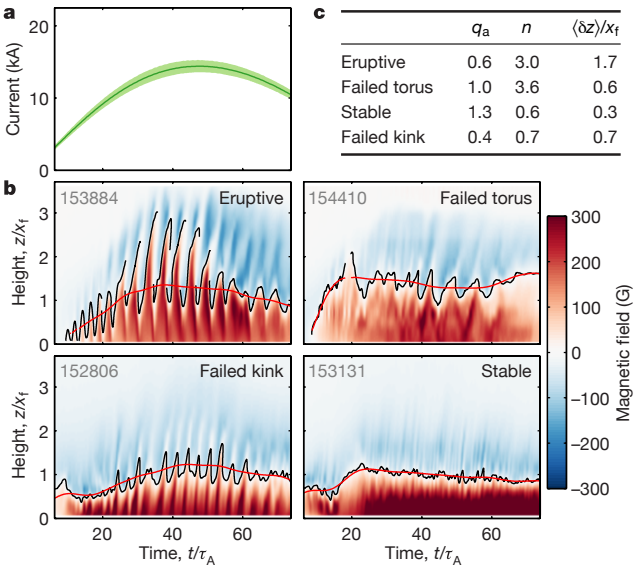

Figure 2. Height-time evolution of four different flux rope discharges. (a) Mean and standard deviation of the nominally identical flux rope current waveforms. (b) Apex height, $z_{ap}(t)$, (black) overlaid on the poloidal magnetic field, $B_P = B_y$, measured for each of the four cases. The equilibrium, or quasi-static, position of the magnetic axis is shown in red. (c) Table of instability parameters for each discharge. This figure reprinted with permission from Ref. 3.

$$q_a \equiv \frac{2\pi}{\iota_a} = \frac{2\pi a}{L}\frac{B_{Ta}}{B_{Pa}} < 1. \tag{2}$$

Here, ι_a is the rotational transform, which measures the field line twist along the length of the flux rope [42]. Additionally, a is the flux rope minor radius, L is the flux rope length, B_{Ta} is the edge toroidal field, and $B_{Pa} \equiv I_T/2\pi a$ is the edge poloidal field, where I_T is the toroidal flux rope current. Here, we assume that B_{Ta} is the vacuum field and that I_T is 90% of the power supply current, giving a 10% uncertainty in q_a (see Ref. 3). For each laboratory flux rope discharge, the instability control parameters n and q_a are evaluated at the maximum flux rope equilibrium height (the maximum of the red traces in Fig. 2b). The resulting values of n and q_a for the four discharges in Fig. 2b are listed in Fig. 2c.

The discharge-by-discharge analysis in Fig. 2 can be applied to all of the flux rope plasmas in the MRX database. The results of this extended analysis are shown in Fig. 3, which plots flux rope eruptivity across the torus versus kink (n vs. q_a) instability parameter space. The color in the plot corresponds to the normalized instability amplitude, $\langle\delta z\rangle/x_f$, which is a metric developed to quantify the eruptivity of a given flux rope. Here, the instability amplitude, $\langle\delta z\rangle$, is defined as the maximum of the envelope of the dynamic spatial oscillations about the equilibrium position of

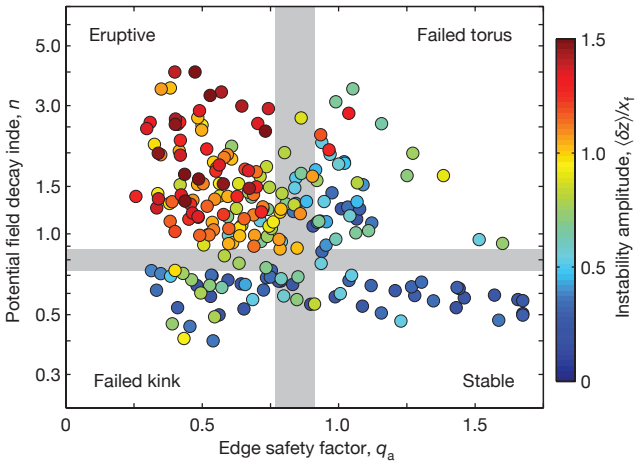

Figure 3. The torus versus kink (n vs. q_a) instability parameter space. The normalized instability amplitude, $\langle \delta z \rangle / x_f$, which represents the spatial extent of the dynamic evolution of the flux rope, is shown in color. Each point in the scatterplot contains 2–5 flux rope discharge taken with identical experimental settings such that more than 800 discharges are represented. The stable, eruptive, and failed kink regimes are expected, but the failed torus regime constitutes a new discovery. This figure reprinted with permission from Ref. 3.

the flux rope. This instability amplitude is normalized to the footpoint major radius, x_f. Values of $\langle \delta z \rangle / x_f$ for the four discharges in Fig. 2b are listed in Fig. 2c.

Four distinct stability regimes are identified in Fig. 3, with the gray bars representing the empirical boundaries between them. The stable and eruptive regimes are anticipated in that both the torus and kink instabilities are (de)stabilized at (high) low n and (low) high q_a. The failed kink regime is also anticipated in that it is qualitatively consistent with numerical simulations of line-tied flux ropes [37]. Here, the kink instability is present, but it saturates at low amplitude. The conclusion is that, without the torus instability, the kink alone cannot drive an eruption. The surprisingly low torus instability threshold of $n \sim 0.8$ is discussed in Section 4. The fourth and final regime in Fig. 3 is the failed torus regime, which constitutes a new discovery. In this regime, flux ropes that are otherwise torus unstable (high n) fail to erupt. As will be described, this behavior is due to a previously unknown dynamic magnetic tension force that prevents the flux rope from erupting.

3. Quasi-static and dynamic tension forces

The laboratory observations presented in the previous section show that the flux rope can persist in a quasi-static equilibrium (Fig. 2) and that unexpected stability can be found in the failed torus regime (Fig. 3). Both of these phenomena are linked to the toroidal field tension force that is the focus of this paper. In this section, we summarize our experimental results on the quasi-static and dynamic components of the toroidal field tension force. We then investigate the parameter dependences and the origins of these two tension force contributions.

In order to study the toroidal field tension force in the laboratory, the various force terms that act on the flux rope must be directly measured from the experimental data. The key force terms and the force measurement procedure are describe elsewhere in full detail [3, 4], so we only briefly summarize them here. In all, three force terms are considered: (1) the upwardly directed hoop force; (2) the downwardly directed strapping force; and (3) the downwardly directed toroidal field tension force.

The hoop force is a poloidal-field-generated force that is derived from the toroidal curvature of the flux rope. Increased magnetic pressure on the inside of the rope and decreased pressure on the outside results in a net upward force. Shafranov [43] gives the hoop force expression in the large aspect ratio limit to be

$$F_h = \frac{\mu_0 I_T^2}{4\pi R}\left[\ln\left(\frac{8R}{a}\right) - 1 + \frac{\ell_i}{2}\right], \tag{3}$$

where I_T is the toroidal current in the flux rope, R is the major radius, a is the minor radius, and ℓ_i is the normalized internal inductance. This expression is derived for a toroidally symmetric ring of current such that corrections are necessary for the non-circular shape of a line-tied flux rope [4].

The strapping force is a poloidal-field-generated restoring force that is due to the interaction between the flux rope toroidal current, I_T, and the vacuum strapping field, B_s:

$$F_s = \mathbf{I}_T \times \mathbf{B}_s = -I_T B_s. \tag{4}$$

Here the strapping force is written with an explicit negative sign such that I_T and B_s are positive-definite.

The final force term is the toroidal field tension force. Much like the hoop force, the tension force is derived from the toroidal curvature of the flux rope. The key field component for the tension force is the internal toroidal field, B_{Ti}. This magnetic field component arises in the cross-section of the flux rope in order to achieve minor radius force balance. In low-β (low thermal pressure) systems such as our laboratory experiments and the solar corona, B_{Ti} is paramagnetic with respect to the vacuum toroidal guide field, B_g. This paramagnetism creates a minor radius magnetic pressure gradient that opposes the minor radius pinch force generated by the toroidal flux rope current.

When bent into an arch, the paramagnetic internal toroidal field, B_{Ti} and its associated poloidal currents, J_P, interact to produce a strong downward force on the inside of the rope and a weak upward force on the outside. This asymmetry results in a net downward

restoring force on the flux rope. As derived in Ref. [4], the tension force can be expressed as

$$F_t \simeq -\frac{1}{2}(\pi a^2)\left[\frac{\langle B_T^2\rangle - B_g^2}{\mu_0 R_c}\right], \tag{5}$$

where $\langle B_T^2\rangle$ is the cross-section averaged square of the total toroidal field and R_c is the radius-of-curvature of the flux rope.

The various force terms described above are measured in the experiment by collecting all three components of the magnetic field, $\mathbf{B}$, and the current density, $\mathbf{J}$, in discharges with the probe array aligned in the poloidal cross-section of the flux rope (see Fig. 1b). The vector magnetic field is measured directly by the probe array, and the toroidal (out-of-plane) current density, J_T, can be computed by taking the curl of the poloidal (in-plane) magnetic field, $\mathbf{B}_P$. If local toroidal symmetry is assumed, then the in-plane current density, $\mathbf{J}_P$, can be computed from the out-of-plane magnetic field, B_{Ti} [4]. With the vector fields and currents in hand, the following equation can be evaluated to convert the volumetric force density, $f \equiv \hat{\mathbf{e}}_z \cdot \mathbf{J} \times \mathbf{B}$, to the force per unit length, F, acting at the flux rope apex, $z = z_{ap}$:

$$F(z_{ap}) = \frac{1}{R_c}\int_0^{2\pi} d\theta \int_0^a dr \left[r\, h_T(z)\, f(r,\theta)\right], \tag{6}$$

Here, θ is the poloidal field coordinate, r is the minor radius coordinate, a is the minor radius, and $h_T(z)$ is the curvilinear scale factor that accounts for the toroidal curvature of the flux rope. The evaluation of this equation is described in full detail in Ref. 4.

Figure 4a shows a comparison of experimentally measured forces to analytical predictions for a characteristic flux rope discharge in MRX. The three experimentally measured force terms are shown as solid patches, while the analytical predictions are shown as solid lines of the same color. The hoop force is positive and pushes upward as expected, while the strapping force and tension force are negative and therefore combine to hold the flux rope in equilibrium. The net sum of the three experimentally measured force terms is shown as a black line. This net sum is approximately zero throughout the discharge, indicating that a force-free equilibrium is measured. With regard to the analytical predictions for this sample discharge, the strapping and tension forces match reasonably well, while the hoop force that is measured is substantially smaller than the hoop force that is predicted.

In Fig. 4b, the experimentally measured force terms are condensed to scalar values that can be used to assess the flux rope force balance. These scalar force values, $\langle F_i\rangle$, are obtained by low-pass filtering and then averaging the corresponding force waveform over the time period where the plasma current is within 5% of its maximum. The dynamic tension force, δF_t,

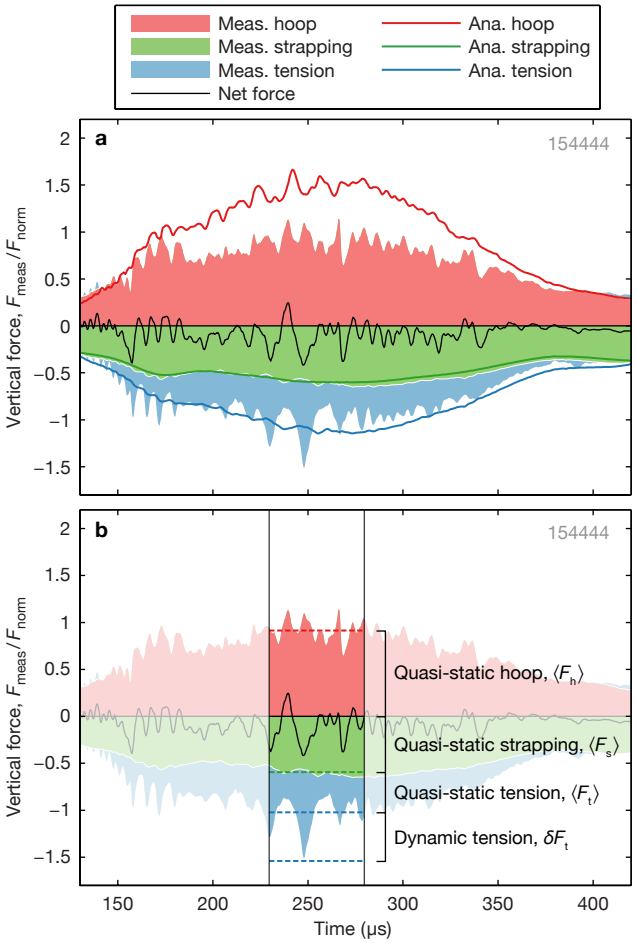

Figure 4. (a) Comparison of experimentally measured (solid patches) and analytically predicted (colored lines) forces for a sample flux rope discharge. The net measured force is shown in black. The forces are normalized to $F_{\rm norm} \equiv \mu_0 I_T^2/4\pi x_f$, where I_T is the toroidal plasma current and $2x_f$ is the footpoint separation distance. A force-free equilibrium is measured, which confirms that these experiments are low-β. The measured hoop force is weaker than the analytical prediction, while the tension and strapping forces are comparable. (b) The various force terms are condensed to scalar values by averaging over the time when the plasma current is within 5% of its maximum. Regarding the tension force, the quasi-static contribution, $\langle F_t\rangle$, is the average of the low-pass-filtered tension force, while the dynamic contribution, δF_t, is the maximum transient in excess of $\langle F_t\rangle$. In this example, δF_t is larger in magnitude than $\langle F_t\rangle$, indicating that the dynamic tension force can be significant.

on the other hand, represents the maximum difference between the measured tension force waveform, $F_t(t)$, and its quasi-static average, $\langle F_t\rangle$. As Fig. 4b shows, the dynamic tension force can match and even exceed the magnitude of the quasi-static tension force.

The force analysis techniques introduced here can be applied across the MRX flux rope database to assess statistical trends in the forces. First, it is desirable to conduct a database-wide comparison between analytical predictions and experimental measurements of the quasi-static forces. As shown in Fig. 5,

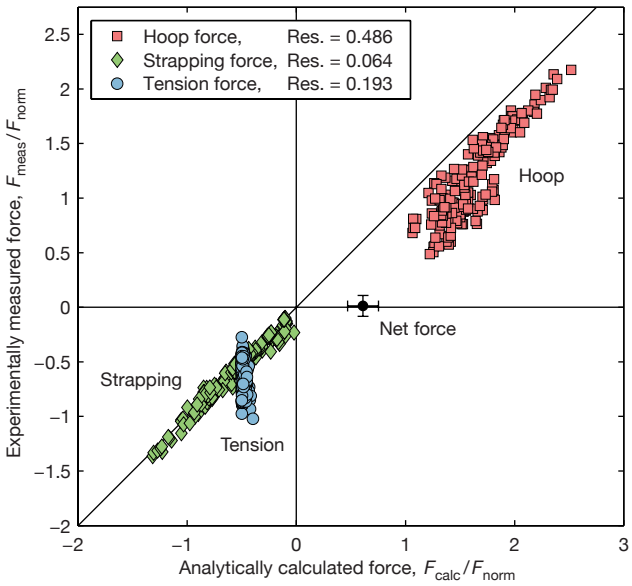

Figure 5. Comparison of measured and predicted quasi-static flux rope forces. Again, the forces are normalized to $F_{\rm norm} \equiv \mu_0 I_T^2/4\pi x_f$. The measured hoop force is weaker than predicted, the strapping force is well-predicted, and the tension force can exceed predicted values by as much as a factor of two. When the various force terms are summed, a force-free equilibrium (zero net force) is measured but not predicted. This figure reprinted with permission from Ref. 4.

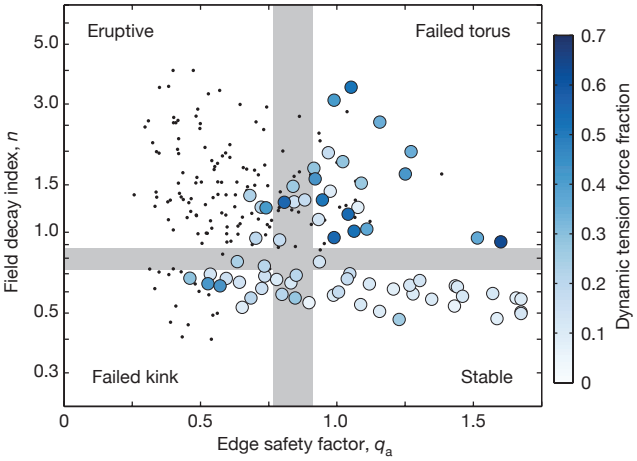

Figure 6. Parameter dependence of the dynamic toroidal field tension force. The dynamic tension force fraction, $\delta F_t/[\langle F_s\rangle + \langle F_t\rangle]$, is plotted over the same n vs. q_a instability parameter space that is shown in Fig. 3. The black dots are the data points where no force measurements are available due to either probe alignment or flux rope volatility. Each viable data point contains 2–5 flux rope discharges. Interestingly, the dynamic tension force is most prevalent in the failed torus regime, somewhat noticeable in the failed kink regime, and entirely absent from the stable flux rope regime.

the trend of a weaker-than-expected hoop force holds consistently across the database, while the strapping field is well-predicted throughout. The quasi-static tension force, on the other hand, is sometimes well-predicted, though it can often exceed its analytical prediction by as much as a factor of two. The quasi-static tension force, which is often ignored in solar eruption models, contributes substantially to the force balance in all of the MRX flux rope equilibria [4].

Next, the three quasi-static force terms can be summed to determine the net force in each flux rope discharge. The single black dot with error bars in Fig. 5 shows the aggregate measured and predicted net force. We see that, to within error bars, a net force of zero is measured experimentally, but that a net positive force is predicted analytically. This implies that the theoretical equilibria are predicted to evolve toward higher altitudes than are observed in the laboratory. This disparity persists in spite of efforts to compensate for the line-tied shape of the flux rope [4]. As such, we conclude that additional low-aspect-ratio and line-tying effects are responsible for the lower altitude equilibria that are observed experimentally. The fact that a net force-free equilibrium is measured in the experiments confirms the assumption that these laboratory flux ropes, like those in the solar corona, are low-β and therefore dominated by $\mathbf{J}\times\mathbf{B}$ forces.

With the quasi-static force analysis in hand, the final task is to investigate the impact of the dynamic toroidal field tension force, δF_t, on the flux rope behavior. To this end, in Fig. 6, we examine the dynamic tension force fraction, which is defined as:

$$\text{Dynamic tension fraction} \equiv \frac{\delta F_t}{\langle F_s\rangle + \langle F_t\rangle}. \qquad (7)$$

This ratio between the dynamic component of the tension force, δF_t, and the total quasi-static restoring force, $\langle F_s\rangle + \langle F_t\rangle$, reveals the parameter regimes where the dynamic tension force contributes significantly to the total force on the flux rope. The axes in Fig. 6 represent the same n vs. q_a parameter space that is defined in Fig. 3. The black dots in Fig. 6 are data points where force measurements are not available due to either the probe alignment or flux rope volatility. Among the viable data points, which each contain measurements from 2–5 flux rope discharges, it is clear that the dynamic tension force can be quite large, and that in many cases it reaches a substantial fraction of the total quasi-static restoring force (strapping + tension). In terms of parameter regimes, Fig. 6 reveals the following: (1) that the dynamic tension force contributes most prominently in the failed torus regime; (2) that it plays a lesser role in the failed kink regime; and (3) that it is absent altogether in the stable flux rope regime. The concentration of the dynamic tension force in the failed torus regime hints that this force may be the key to the unexpected lack of eruptivity observed in the experiments.

To demonstrate that the dynamic tension force is

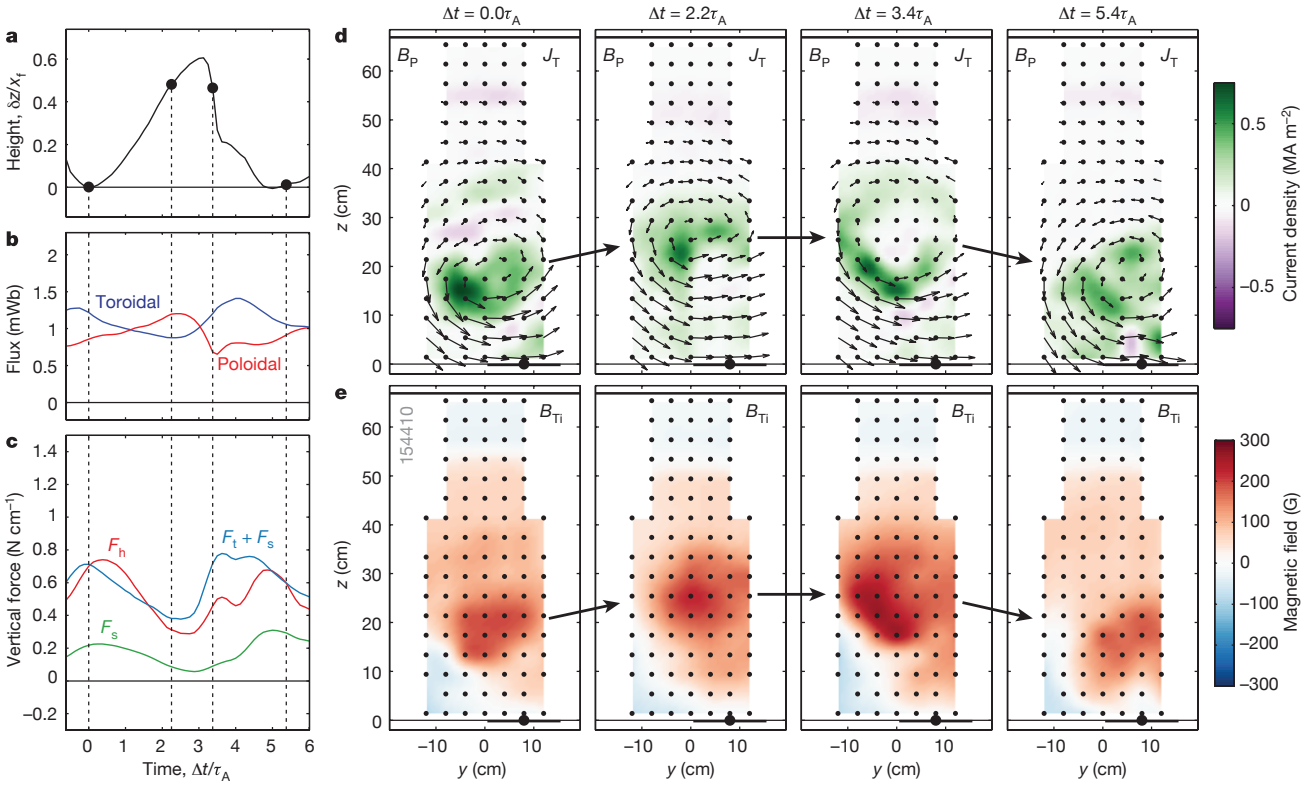

Figure 7. Analysis of a characteristic failed torus event. (a) Height-time trace showing that the flux rope initially rises before abruptly saturating and collapsing back to its initial location. (b) Comparison of toroidal and poloidal fluxes showing the rapid exchange of poloidal and toroidal fluxes during the failed torus event. (c) Comparison of flux rope forces showing the initial dominance of the hoop force that is overtaken by the dynamic toroidal field tension force, which causes the event to fail. (d)/(e) Toroidal current density, J_T, and internal toroidal field, B_{Ti}, profiles showing the internal reconfiguration of the flux rope. Simultaneously, the J_T profile hollows out and the B_{Ti} profile is enhanced, giving rise to the dynamic tension force that halts the rise of the flux rope. This figure reprinted with permission from Ref. 3.

the key physical mechanism that prevents eruptions in the failed torus regime, we now examine the flux rope evolution during a characteristic failed torus event. Figure 7 shows one such event, which evolves over just a few Alfvén times, τ_A. First, in Fig. 7a, the spatial evolution of the failed torus event shows that the flux rope initially rises before saturating and then abruptly collapsing back to its initial position. In Fig. 7d, four spatial snapshots of the poloidal magnetic field, $\mathbf{B}_P$, and the corresponding toroidal current density, J_T, show that the flux rope undergoes an internal reconfiguration during the failed torus event. In particular, the initially uniform J_T profile becomes strikingly hollow. At the same time, the paramagnetic internal toroidal field, B_{Ti}, is transiently enhanced (see Fig. 7e). This transiently enhanced B_{Ti} produces the dynamic toroidal field tension force.

The hollowing of J_T and the enhancement of B_{Ti} can best be understood by examining the toroidal and poloidal magnetic fluxes entrained in the flux rope (see Fig. 7b). Initially, the toroidal flux decreases and the poloidal flux increases as the flux rope rises. When the current profile hollows out, however, there is a rapid exchange of toroidal and poloidal fluxes. This exchange is interpreted as the signature of a magnetic self-organization event [44, 45] wherein magnetic reconnection facilitates the internal reconfiguration of the flux rope [3]. The details of the self-organization process in these flux ropes are investigated more closely in Yamada et al. [46]. The key concept is that flux ropes in the failed torus regime can find a lower energy state through internal self-organization rather than external eruption.

Lastly, the $\mathbf{J} \times \mathbf{B}$ force measurement techniques described earlier in the paper can be used to assess the impact of the magnetic self-organization process on the flux rope forces. In Fig. 7c, the absolute values of the three force terms are compared. Initially, the hoop force exceeds the combined strapping + tension restoring force. During the self-organization event, however, the enhanced B_{Ti} generates a very large dynamic toroidal field tension force that overtakes the hoop force and prevents the flux rope from erupting. In this way, the dynamic toroidal field tension force that is observed throughout the failed torus regime in Fig. 6 is the direct cause of the unexpected failed torus

behavior that is observed in MRX.

4. Summary and discussion

In this paper, we report on the key role of both quasi-static and dynamic magnetic tension forces in the equilibrium and stability of line-tied magnetic flux ropes. These forces are studied in a laboratory experiment that is expressly designed to produce quasi-statically evolving flux ropes that may be driven to erupt by ideal magnetohydrodynamic instabilities such as the kink and torus instabilities. Four different stability regimes are observed in the experiment. The failed torus regime, where nominally torus-unstable flux ropes fail to erupt, constitutes a new discovery.

Direct measurements of the flux rope forces provide a deep understanding of the role of the quasi-static and dynamic tension forces. First, the quasi-static tension force contributes a restoring force that is of the same order as the strapping force in all of the measured laboratory equilibria. Furthermore, this quasi-static tension force can exceed analytical predictions by as much as a factor of two. As such, the quasi-static tension force must be considered in loss-of-equilibrium solar eruption models. The dynamic tension force, on the other hand, has an even more profound impact in the failed torus regime where it prevents the flux rope from erupting. Measurements show that magnetic self-organization events reconfigure the internal structure of the flux rope, thereby creating a transiently enhanced paramagnetic toroidal field and a corresponding dynamic toroidal field tension force. This dynamic tension force overtakes the hoop force and halts the eruption.

In the effort to connect these laboratory results to events in the solar corona, several experimental factors must be considered. First, the laboratory flux rope and power supply circuit differs from the solar case in that there is a large external series inductance in the laboratory that largely maintains the flux rope current during an eruption. In the solar case, on the other hand, the current is expected to drop as the rope expands in order to conserve poloidal flux [19]. Thus, the quasi-current-source behavior in the laboratory, in concert with the partial torus instability considerations of Olmedo & Zhang [40], contributes to the observed $n \sim 0.8$ torus instability threshold.

A second consequence of the series inductance in the laboratory circuit is that a large inductive electric field persists following the eruption and ejection of a flux rope. This latent inductive electric field is likely responsible for the rapid reformation and re-eruption of the flux rope plasma that is observed in the eruptive regime (see Fig. 2b). A further consideration is that the inductive electric field and the proximity of vessel wall are likely to influence how the flux rope detaches in the later stages of the eruption. These considerations argue for future experiments with a larger chamber and a modified power supply with a smaller inductance and larger capacitance to elucidate these phenomena.

A final consideration for future work is to develop a better understanding of the magnetic self-organization process observed here. Though some evidence for an internal reconfiguration via magnetic reconnection has been identified [46], the reconnection process has yet to be measured directly. Furthermore, the threshold for failed torus events independent of the kink instability should be identified. This is likely to involve further investigations of the role of magnetic helicity in this phenomenon, possibly through dedicated numerical simulations. Regardless, it is clear that the enhanced toroidal magnetic field and the resulting dynamic magnetic tension force that it generates can cause torus-driven flux rope eruptions to fail. This dynamic tension force is not accounted for in standard solar eruption models and therefore must be added to improve our ability to interpret and eventually predict solar eruptive events.

Acknowledgements

The authors thank R. Cutler, E. E. Lawrence, F. Scotti, P. Sloboda, and T. D. Tharp for technical contributions and R. M. Kulsrud for useful discussions. This research is supported by Department of Energy (DoE) contract number DE-AC02-09CH11466 and by the National Science Foundation/DoE Center for Magnetic Self-Organization (CMSO). The digital data for this paper can be found at `http://dataspace.princeton.edu/jspui/handle/88435/dsp01x920g025r`.

[1] Wesson J 1987 *Tokamaks* (Oxford: Clarendon Press)
[2] Miyamoto K 2005 *Plasma Physics and Controlled Nuclear Fusion* (New York: Springer)
[3] Myers C E, Yamada M, Ji H, Yoo J, Fox W, Jara-Almonte J, Savcheva A and DeLuca E E 2015 *Nature* **528** 526–529
[4] Myers C E, Yamada M, Ji H, Yoo J, Jara-Almonte J and Fox W 2016 *Phys. Plasmas* Under review.
[5] Amari T, Canou A and Aly J J 2014 *Nature* **514** 465–469
[6] Kuperus M and Raadu M A 1974 *Astron. Astrophys.* **31** 189–193
[7] Chen J 1989 *Astrophys. J.* **338** 453–470
[8] Low B C 2001 *J. Geophys. Res.* **106** 25141
[9] Forbes T, Linker J, Chen J, Cid C, Kóta J, Lee M, Mann G, Mikić Z, Potgieter M, Schmidt J, Siscoe G, Vainio R, Antiochos S and Riley P 2006 *Space Sci. Rev.* **123** 251–302
[10] Green L M and Kliem B 2009 *Astrophys. J. Lett.* **700** L83
[11] Aschwanden M J 2006 *Physics of the Solar Corona* (Springer)
[12] Kunow H, Crooker N U, Linker J A, Schwenn R and von Steiger R (eds) 2006 *Coronal Mass Ejections* (Springer) ch. 2, 12

[13] Pulkkinen T 2007 *Living Rev. Solar Phys.* **4** URL `http://www.livingreviews.org/lrsp-2007-1`
[14] Kruskal M and Schwarzschild M 1954 *Proc. R. Soc. Lond. A* **223** 348–360
[15] Shafranov V 1956 *Sov. J. At. Energy* **1** 709–713
[16] Gold T and Hoyle F 1960 *Mon. Not. R. Astron. Soc.* **120** 89–105
[17] Hood A W and Priest E R 1981 *Geophys. Astrophys. Fluid Dyn.* **17** 297–318
[18] Bateman G 1978 *MHD Instabilities* (MIT Press)
[19] Kliem B and Török T 2006 *Phys. Rev. Lett.* **96** 255002
[20] Rust D M and Kumar A 1996 *Astrophys. J. Lett.* **464** L199
[21] Ji H, Wang H, Schmahl E J, Moon Y J and Jiang Y 2003 *Astrophys. J. Lett.* **595** L135–L138
[22] Cheng X, Ding M D, Zhang J, Srivastava A K, Guo Y, Chen P F and Sun J Q 2014 *Astrophys. J. Lett.* **789** L35
[23] Zuccarello F P, Seaton D B, Mierla M, Poedts S, Rachmeler L A, Romano P and Zuccarello F 2014 *Astrophys. J.* **785** 88
[24] Savcheva A S, van Ballegooijen A A and DeLuca E E 2012 *Astrophys. J.* **744** 78
[25] Yan X L, Xue Z K, Liu J H, Ma L, Kong D F, Qu Z Q and Li Z 2014 *Astrophys. J.* **782** 67 (*Preprint* `1401.0244`)
[26] Sakurai T 1976 *Publ. Astron. Soc. Japan* **28** 177–198
[27] Mikić Z, Schnack D D and van Hoven G 1990 *Astrophys. J.* **361** 690–700
[28] Amari T, Luciani J F, Aly J J, Mikić Z and Linker J 2003 *Astrophys. J.* **585** 1073
[29] T Török, B Kliem and V S Titov 2004 *Astron. Astrophys.* **413** L27–L30
[30] Fan Y and Gibson S E 2007 *Astrophys. J.* **668** 1232–1245
[31] Aulanier G, Török T, Démoulin P and DeLuca E E 2010 *Astrophys. J.* **708** 314
[32] Myers C E 2015 *Laboratory Study of the Equilibrium and Eruption of Line-Tied Magnetic Flux Ropes in the Solar Corona* Ph.D. thesis Princeton University URL `http://arks.princeton.edu/ark:/88435/dsp01dv13zw44b`
[33] Yamada M, Ji H, Hsu S, Carter T, Kulsrud R *et al.* 1997 *Phys. Plasmas* **4** 1936–1944
[34] Hansen J F and Bellan P M 2001 *Astrophys. J.* **563** L183–L186
[35] Tripathi S K P and Gekelman W 2010 *Phys. Rev. Lett.* **105** 075005
[36] Soltwisch H, Kempkes P, Mackel F, Stein H, Tenfelde J, Arnold L, Dreher J and Grauer R 2010 *Plasma Phys. Control. Fusion* **52** 124030
[37] Török T and Kliem B 2005 *Astrophys. J.* **630** L97–L100
[38] Liu Y 2008 *Astrophys. J. Lett.* **679** L151–L154
[39] Démoulin P and Aulanier G 2010 *Astrophys. J.* **718** 1388–1399
[40] Olmedo O and Zhang J 2010 *Astrophys. J.* **718** 433–440
[41] Savcheva A, Pariat E, van Ballegooijen A, Aulanier G and DeLuca E 2012 *Astrophys. J.* **750** 15
[42] Freidberg J P 1987 *Ideal Magnetohydrodynamics* (Plenum Press)
[43] Shafranov V 1966 Plasma equilibrium in a magnetic field *Rev. Plasma Phys.* vol 2 ed Leontovich M A (New York: Consultants Bureau Enterprises) pp 103–152
[44] Taylor J B 1986 *Rev. Mod. Phys.* **58** 741–763
[45] Ji H, Prager S C and Sarff J S 1995 *Phys. Rev. Lett.* **74**(15) 2945–2948
[46] Yamada M, Yoo J and Myers C E 2016 *Phys. Plasmas* **23** 055402